A pragmatic orthotropic elasticity-based damage model with spatially distributed properties applied to short glass-fibre reinforced polymers

Petter Henrik Holmström [a,b,c,*], Arild Holm Clausen [a,b], Torodd Berstad [a,b], David Morin [a,b], Odd Sture Hopperstad [a,b]

[a] *Structural Impact Laboratory (SIMLab), Department of Structural Engineering, Norwegian University of Science and Technology (NTNU), Trondheim, Norway*
[b] *Centre for Advanced Structural Analysis (CASA), NTNU, Trondheim, Norway*
[c] *Currently at Equinor ASA, Trondheim, Norway*

ARTICLE INFO

ABSTRACT

This article presents a simple progressive damage model for quasi-brittle materials, combining orthotropic elasticity with a scalar damage model including spatial variation of the damage initiation strain and the crack band method for softening regularization. The model's performance is first analyzed from a numerical point of view and then demonstrated for tensile tests ($0°$, $45°$ and $90°$), open-hole tensile tests ($0°$) and three-point bending ($0°$ and $90°$) tests of short fibre-reinforced polypropylene with 15 wt.% and 30 wt.% glass fibres. Despite its simplicity, the model captures the anisotropic elastic and inelastic behaviour observed in experiments. The model is applicable for orthotropic brittle or quasi-brittle materials, where the variability in elastic properties is negligible and the orientation dependency of the fracture strain is small or not relevant for the application.

© 2021 The Author(s). Published by Elsevier Ltd. This is an open access article under the CC BY license (http://creativecommons.org/licenses/by/4.0/).

1. Introduction

Development of phenomenological models for progressive failure of anisotropic materials has been an active area of research for several decades. Applications are found in e.g. the automotive, aeronautical, aerospace and wind energy industry and include brittle and quasi-brittle materials, such as polymer matrix composites (PMCs), metal matrix composites (MMCs), ceramic matrix composites (CMCs) and concrete. The finite element (FE) method is the primary design tool for structural applications involving such materials, but the approach is limited by the predictive capability of available material models. It is therefore of great importance that the industry has access to computationally efficient, robust and sufficiently accurate material models with parameters which are easy to identify from standard tests.

Progressive failure models for quasi-brittle materials are often formulated within the framework of continuum damage mechanics (CDM) and may combine isotropic, transverse isotropic or orthotropic elasticity with a failure initiation criterion and a damage evolution rule. Some frequently applied criteria for describing the onset of material degradation are the maximum stress, maximum strain, Tsai and Wu (1971), Hashin (1980), Puck and Shürmann (1998) and LaRC04 (Pinho et al., 2005) criteria. The damage evolution rule is typically formulated such that linear or exponential strain softening is achieved, where the softening may be controlled by one or several variables depending on the number of modelled failure modes. Examples of studies developing anisotropic progressive damage models include Matzenmiller et al. (1995), who formulated a model combining orthotropic elasticity and the Hashin criterion where damage was related to effective elastic properties, Maimí et al. (2007), who used orthotropic elasticity, a simplified version of the LaRC04 criterion and linear-exponential softening to predict intralaminar failure mechanism in FRP laminates under plane stress, and Lapczyk and Hurtado (2007), who combined orthotropic elasticity with the Hashin criterion and linear softening to predict failure of fibre-reinforced materials. More recent contributions typically present combinations or modifications of previously established ideas, evaluations of existing models or applications to new materials (Simon et al., 2017; Reinoso et al., 2017; Shen et al., 2019; Zhou et al., 2019; Yoon et al., 2019; Gu et al., 2019; Zheng et al., 2020; Wei et al., 2019; Kumar et al., 2019). Most of the models mentioned so far apply the so-called crack band model presented by Bažant and Oh (1983) to deal with the pathological mesh dependency caused by damage-induced strain softening.

Although a material is known to have a heterogeneous structure with stochastic properties, the classical approach is to consider it

---

* Corresponding author.
  E-mail address: petter.h.holmstrom@ntnu.no (P.H. Holmström).

as a homogeneous solid with deterministic properties. To illustrate why this may be inadequate and simultaneously lead to unnecessary modelling complexity, an example from the current study is presented in Fig. 1. The figure shows images of a tensile test specimen of a short fibre-reinforced polymer, where the left part reveals the heterogeneous material structure of fibres and matrix (near the specimen surface), whereas the right part presents the strain field under tensile loading, measured at the surface of the very same sample. The results demonstrate that the strain heterogeneities, which in reality are cracks in the specimen surface (Nouri et al., 2017), evolve on a length scale which is larger than the length scale of the single fibres and comparable to structures in the material such as fibre clusters and regions with low fibre content. An attractive way to represent the observed heterogeneities in a numerical model could be to introduce spatially heterogeneous material properties.

The two main approaches for modelling material heterogeneities in FE simulations are the direct approach, where the material phases are modelled explicitly, and the indirect approach, where the material heterogeneity is obtained by assigning spatially heterogeneous material properties over the structure (Yang et al., 2009). For industrial applications, the indirect approach is particularly appealing due to its simplicity and potential for high computational efficiency. Although spatially heterogeneous material properties have been applied for elastic (Ly et al., 2019), hyperelastic (Mihai et al., 2018; Staber et al., 2019) and micromechanical models (Desrumaux et al., 2001; Jendli et al., 2009; Despringre et al., 2016), it is surprisingly seldom accounted for in FE simulations. However, Yang et al. (2009) simulated two-dimensional crack propagation using cohesive elements with linear softening, where the tensile strength was governed by a spatially varying Weibull field. The method was extended to three dimensions by Su et al. (2010). Monte Carlo simulations were run for a concrete tensile specimen and both the 2D and 3D versions were able to predict rather realistic crack propagation and load-carrying capacity. Naderi and Khonsari (2013) studied progressive intra- and inter-laminar fracture of laminates by combining transverse isotropy with three different damage models and spatially heterogeneous values for the stiffness and strength, assigned from a narrow Gauss distribution. Also here, the fracture paths and load–displacement curves from the simulations were in close agreement with the experiments. Le and Eliáš (2016) showed how probability distributions of the strength of quasi-brittle structures may be achieved by using isotropic elasticity and a scalar damage model with stochastic values of the strength and fracture energy, when the crack band widths are smaller than the finite element size. The studies presented above demonstrate that nonlinearity and fracture may be predicted with relatively high accuracy by introduction of spatially heterogeneous material properties, even without complex model formulations.
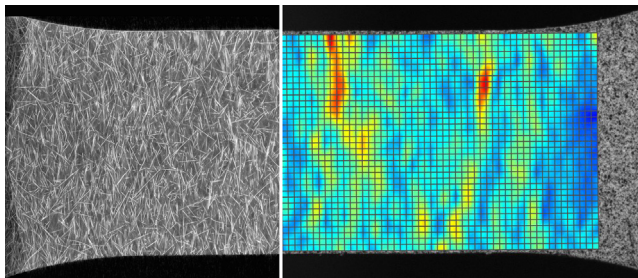

Fig. 1. X-CT image from one of the shell layers of a (90°) tensile test specimen of polypropylene reinforced with 30 wt.% glass fibres (left), and strain field at maximum force for the very same specimen (right), see Nouri et al. (2017) for similar results. The nominal geometry of the specimen is presented in Fig. 4.

The objective of the paper is to present a simple, computationally efficient anisotropic elastic damage model tailored for quasi-brittle materials and industrial applications. To this end, orthotropic elasticity is combined with a scalar damage model where the damage initiation is introduced as a stochastic variable and the softening is linear. Bažant and Oh (1983) regularization procedure is applied to reduce the mesh sensitivity. The proposed model has spatially heterogeneous material properties, and should be regarded as an alternative to complex models with homogeneous material properties. The model's performance is demonstrated for short fibre-reinforced polypropylene, but the modelling approach may be just as relevant for other heterogeneous materials or materials with stochastic properties.

The paper is organized as follows. First, the model is presented in detail and it is outlined how the model may be calibrated for the materials applied in this work. Second, the model is validated against 0°, 45° and 90° tensile tests and, third, a numerical evaluation of the model is presented. Fourth, the model is validated against open-hole tensile tests and three-point bending tests, before the paper is rounded off with perspectives and conclusions. Results are discussed consecutively.

2. Material model

The model is developed for brittle or quasi-brittle materials, where the strains remain small while the rotations can be finite. A corotational stress approach is adopted to obtain an invariant formulation for anisotropic materials, and the corotational stress tensor $\hat{\boldsymbol{\sigma}}$ reads

$$\hat{\boldsymbol{\sigma}} = \boldsymbol{R}^T \cdot \boldsymbol{\sigma} \cdot \boldsymbol{R} \tag{1}$$

where $\boldsymbol{\sigma}$ is the Cauchy stress tensor, and $\boldsymbol{R}$ is the rotation tensor obtained from polar decomposition of the deformation gradient tensor $\boldsymbol{F}$. Correspondingly, the corotational rate-of-deformation tensor $\hat{\boldsymbol{D}}$ is defined as

$$\hat{\boldsymbol{D}} = \boldsymbol{R}^T \cdot \boldsymbol{D} \cdot \boldsymbol{R} \tag{2}$$

where $\boldsymbol{D}$ is the rate-of-deformation tensor.

Orthotropic elasticity is used to describe the anisotropic elastic behaviour. Since the variation in elastic properties is small for most materials and to keep the model as simple as possible, spatially heterogeneous properties are not considered for the elastic part. The orthotropic hypoelastic relation in the corotational framework reads

$$\dot{\hat{\boldsymbol{\sigma}}} = \hat{\mathbf{C}} : \hat{\boldsymbol{D}} \tag{3}$$

where $\hat{\mathbf{C}}$ is the orthotropic elasticity tensor. Using Voigt notation, the matrix form of the anisotropic hypoelastic relation is given by

$$\begin{bmatrix} \dot{\hat{\sigma}}_{11} \\ \dot{\hat{\sigma}}_{22} \\ \dot{\hat{\sigma}}_{33} \\ \dot{\hat{\sigma}}_{23} \\ \dot{\hat{\sigma}}_{31} \\ \dot{\hat{\sigma}}_{12} \end{bmatrix} = \begin{bmatrix} \frac{1}{E_1} & -\frac{v_{21}}{E_2} & -\frac{v_{31}}{E_3} & 0 & 0 & 0 \\ -\frac{v_{12}}{E_1} & \frac{1}{E_2} & -\frac{v_{32}}{E_3} & 0 & 0 & 0 \\ -\frac{v_{13}}{E_1} & -\frac{v_{23}}{E_2} & \frac{1}{E_3} & 0 & 0 & 0 \\ 0 & 0 & 0 & \frac{1}{G_{23}} & 0 & 0 \\ 0 & 0 & 0 & 0 & \frac{1}{G_{31}} & 0 \\ 0 & 0 & 0 & 0 & 0 & \frac{1}{G_{12}} \end{bmatrix}^{-1} \begin{bmatrix} \hat{D}_{11} \\ \hat{D}_{22} \\ \hat{D}_{33} \\ 2\hat{D}_{23} \\ 2\hat{D}_{31} \\ 2\hat{D}_{12} \end{bmatrix} \tag{4}$$

where the elastic coefficients E_i, G_{ij} and v_{ij} are the Young's moduli, shear moduli and Poisson's ratios, respectively. Due to the orthotropic symmetry (Irgens, 2008), we have the relations

$$\frac{v_{12}}{E_1} = \frac{v_{21}}{E_2}, \qquad \frac{v_{13}}{E_1} = \frac{v_{31}}{E_3}, \qquad \frac{v_{23}}{E_2} = \frac{v_{32}}{E_3} \tag{5}$$

and only nine of the twelve elastic coefficients in $\hat{\mathbf{C}}$ are independent.

Damage coupling is obtained by substituting the corotational stress tensor $\hat{\boldsymbol{\sigma}}$ with an effective corotational stress tensor $\hat{\boldsymbol{\sigma}}_{\text{eff}}$ in all constitutive equations according to

$$\hat{\boldsymbol{\sigma}}_{\text{eff}} = \frac{\hat{\boldsymbol{\sigma}}}{1 - D} \tag{6}$$

where $0 \leqslant D < 1$ is the scalar damage variable. A critical damage value $D_c = 0.98$ is introduced to define failure of the material, here realized by element erosion. An equivalent deformation measure, which we need for the damage evolution law, is defined as (Mazars, 1986)

$$\bar{\varepsilon}_{\text{D}} = \sqrt[a_{\text{f}}]{\sum_{i=1}^{3} \langle \hat{\varepsilon}_i \rangle^{a_{\text{f}}}} \tag{7}$$

where a_{f} is a model parameter (typically set to 2), $\hat{\varepsilon}_i$ are the principal values of the corotational deformation tensor $\hat{\boldsymbol{\varepsilon}}$ and $\langle \cdot \rangle$ is the Macaulay bracket, setting negative arguments to zero. As the equivalent deformation measure in Eq. (7) only accounts for the positive principal values of $\hat{\boldsymbol{\varepsilon}}$, damage evolution is limited to strain states with tensile strain in at least one of the principal directions. The corotational deformation tensor $\hat{\boldsymbol{\varepsilon}}$ is obtained from time integration of the corotational rate-of-deformation tensor $\hat{\boldsymbol{D}}$ (Stören and Rice, 1975), viz.

$$\hat{\boldsymbol{\varepsilon}}(t) = \int_0^t \hat{\boldsymbol{D}} dt \tag{8}$$

The internal history variable governing damage evolution is denoted κ and is defined in terms of $\bar{\varepsilon}_D$ by loading–unloading conditions in Kuhn-Tucker form

$$f_D = \bar{\varepsilon}_D - \kappa \leq 0, \quad \dot{\kappa} \geqslant 0, \quad \dot{\kappa} f_D = 0 \tag{9}$$

where f_D is the damage loading function (de Borst and Verhoosel, 2017) and κ is the largest observed value of the equivalent deformation measure $\bar{\varepsilon}_D$ throughout the loading history. Hence, the material remembers the most critical state, and the damage only

grows when this state is exceeded. A positive threshold value κ_0 is introduced for κ, defined such that damage growth is limited to $\kappa \geqslant \kappa_0$. We will refer to κ_0 as the damage initiation parameter and, later, we will define κ_0 as a stochastic variable. The selected damage evolution law is among others used by Song et al. (2008), and reads

$$D(\kappa) = \begin{cases} 0 & \text{for } \kappa < \kappa_0 \\ 1 - \frac{\kappa_0}{\kappa_1 - \kappa_0}\left(\frac{\kappa_1}{\kappa} - 1\right) & \text{otherwise} \end{cases} \tag{10}$$

where κ_1 is a model constant ($\kappa_1 > \kappa_0$), which defines the slope of the descending branch of the stress–strain curve. The damage model is visualized in Fig. 2a for the special case of uniaxial tension, where the history variable κ equals the tensile strain ε. Note that the damage evolution law is formulated such that the material experiences linear softening for $\kappa \geqslant \kappa_0$. Another feature associated with Eq. (9) is that no damage is accumulated during unloading.

The regularization procedure presented by Bažant and Oh (1983), often referred to as the *crack band model*, is applied to reduce the mesh sensitivity of the model. In this approach, the energy dissipated by the material in an element, calculated as the area under the stress–strain curve multiplied with the volume of the element V_{el}, is related to the energy dissipated to generate new surfaces in the material, calculated as the fracture energy G_{f} [N/mm] multiplied with the area of the fractured surface A_{el}. This implies that

$$\frac{1}{2} E \kappa_0 \kappa_1 V_{\text{el}} = G_{\text{f}} A_{\text{el}} \tag{11}$$

where E is the relevant Young's modulus for the actual loading. In the model presented here, we have chosen a pragmatic approach where the fracture energy G_{f} is considered as a direction-independent parameter rather than a material property. By assuming cube-shaped finite elements with characteristic element length h_{el} ($A_{\text{el}} = h_{\text{el}}^2$ and $V_{\text{el}} = h_{\text{el}}^3$), we obtain an expression for κ_1 as
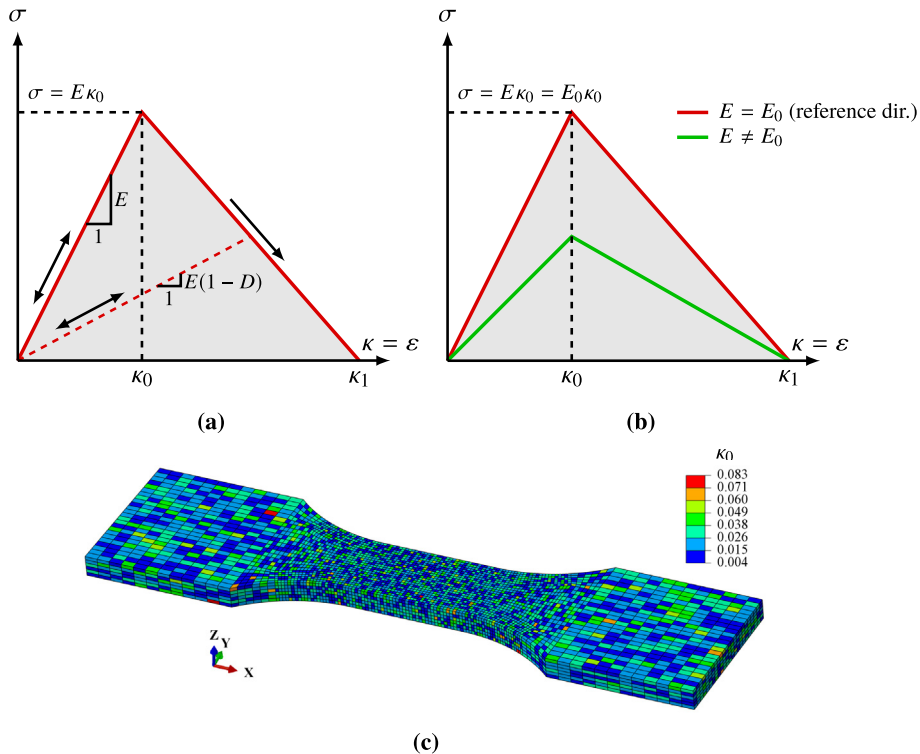

(a)

(b)

(c)

Fig. 2. (a) Stress–strain curve with unloading for the material model in uniaxial tension, where E is Young's modulus in the applied tensile direction. (b) Stress–strain curves for two different tensile directions, where E_0 (red) is the reference direction of the orthotropic material and E (green) is some other direction. (c) FE model of a tensile test specimen with assigned values of the damage initiation parameter κ_0.

$$\kappa_1 = \frac{2G_f}{E\kappa_0 h_{el}} \tag{12}$$

To simplify the regularization procedure further, the variable E is replaced with a fixed model parameter E_0 such that Eq. (12) takes the form

$$\kappa_1 = \frac{2G_f}{E_0 \kappa_0 h_{el}} \tag{13}$$

The value of the parameter E_0 is typically set equal to Young's modulus E_1 along the first principal axis of the orthotropic material. It is further noted that if κ_0 is fixed, Eq. (13) provides an explicit expression for κ_1 as function of known parameters. The characteristic element length h_{el} applied in this work is a default value provided by the finite element software (Abaqus 6.14, 2014) and the value computed in the first time step is used throughout the simulation. Since the model is intended to be used for quasi-brittle materials, only experiencing small strains, the shape of the elements and hence h_{el} will not change much during the simulation. It is also emphasized that cubical elements should be used in the critical parts of the structure where failure is expected to occur, while non-cubical elements may be used elsewhere to save computational time.

Fig. 2b illustrates the model behaviour in uniaxial tension for two different material orientations. Because the values of κ_0 and κ_1 are independent of material orientation, the softening modulus is lower for the softer material orientations compared to the stiffer. The presented damage model is therefore well-suited for quasi-brittle materials which show similar fracture strains for all load directions or for applications where the anisotropy of the fracture behaviour is of minor importance.

The stochastic nature of composite materials is particularly evident when considering the fracture process. We will now introduce randomness to the model, but only one variable will be made stochastic to keep the model as simple as possible. The natural choice is the damage initiation parameter κ_0, which is an indirect measure of the material strength. As illustrated in Fig. 2c, spatially heterogeneous κ_0 values are assigned to the FE model to mimic a heterogeneous material. The length scale over which we assign the κ_0 values is not arbitrary and should be adjusted to the material at hand, a topic which is further addressed in Section 5.2. For the materials applied in this work, this characteristic length scale could be the length scale over which the strain heterogeneities evolve in Fig. 1. A left-truncated normal distribution function $g_{LTN}(\kappa_0)$ is applied for the damage initiation parameter κ_0, which both ensures a well-defined transition from purely elastic to damaged material and avoids negative κ_0 values. A normally-distributed parameter κ_0 is adopted with probability density function $g(\kappa_0)$ defined by

$$g(\kappa_0) = \frac{1}{\kappa_{0,std}\sqrt{2\pi}} \exp\left[-\frac{1}{2}\left(\frac{\kappa_0 - \kappa_{0,mean}}{\kappa_{0,std}}\right)^2\right] \tag{14}$$

The probability density function of the left-truncated normal distribution is then given by

$$g_{LTN}(\kappa_0) = \begin{cases} 0 & \kappa_0 < \kappa_{0,min} \\ \frac{g(\kappa_0)}{\int_{\kappa_{0,min}}^{\infty} g(\kappa_0)d\kappa_0} & \kappa_0 \geqslant \kappa_{0,min} \end{cases} \tag{15}$$

where $\kappa_{0,mean}$, $\kappa_{0,std}$ and $\kappa_{0,min}$ are the mean value, standard deviation and left-truncation value, respectively.

The material model is implemented as a user-defined material model (VUMAT) in Abaqus/Explicit, where the explicit solver was applied for its robustness in handling element erosion to simulate fracture. The anisotropic elastic part of the material model was ver-ified against the material model for orthotropic elasticity available in Abaqus.

3. Materials and model calibration

Three materials are investigated in this work: an unreinforced polypropylene (PP), a polypropylene with 15 wt.% E-glass fibres (PP15) and a polypropylene with 30 wt.% E-glass fibres (PP30), where the PP15 is a blend of the PP and PP30 materials. All materials were delivered as injection-moulded plates with nominal thickness 2.7 mm. According to the producer, the materials are specially developed for use in thin-walled injection-moulded parts. Results from fibre weight fraction measurements (performed by SINTEF Industry, Oslo, Norway) were close to the nominal values both for PP15 and PP30. For both materials, X-ray computed tomography scans were used to estimate the fibre diameter and mean length to, respectively, 20 µm and around 900 µm (Holmström, 2019).

The orthotropic elastic part of the model is calibrated for the fibre-reinforced materials by following the procedure explained in Holmström et al. (2020). This procedure requires tensile tests in the $0°, 45°$ and $90°$ directions of the composite material, see Fig. 3a for angle definition, in addition to one tensile test of the unreinforced polymer. Table 1 presents the values of the calibrated engineering constants, obtained from the experimental results presented in the forthcoming Section 4.2. The calibrated (analytical) orthotropic model is compared with the experimental results in Figs. 3b-d, where the equations for plotting the engineering constants as function of angle are given in e.g. (Holmström et al., 2020). Orthotropic elasticity is, evidently, an excellent approximation for the fibre-reinforced materials investigated in this work. Equivalent results have been reported for similar materials (De Monte et al., 2010; Mortazavian and Fatemi, 2015; Ayadi et al., 2016).

One single tensile test is sufficient to calibrate the damage part of the model, as long as the scatter between replicate tests is small. The parameters E_0, a_f and $\kappa_{0,min}$ are straightforward to determine. The value of E_0 is set equal to E_1 of the orthotropic material and the natural choice of the parameter a_f is 2 (see Eq. (7)). The left-truncation $\kappa_{0,min}$ of the damage initiation distribution defines the end of the purely elastic regime, and the value of this parameter may be set to the strain corresponding to the onset of the nonlinear response observed in the experiments. A reverse engineering approach must, however, be applied for the parameters G_f, $\kappa_{0,mean}$ and $\kappa_{0,std}$, typically by comparing results from FE simulations of the tensile test with one or more experiments. For each of the two fibre-reinforced materials investigated herein, the damage part of the model was calibrated to one representative tensile test in the reference direction ($\theta = 0°$). The resulting calibrated parameters of the damage part of the model are given in Table 2.

Application of reverse engineering implies that the finite element formulation affects the calibration process. As will be discussed in Section 5.2, the number of integration points and the element size are also model parameters since they determine the physical length scale over which we assign the values of the damage initiation parameter (κ_0). An appropriate finite element size was determined by running tensile test simulations with a roughly calibrated material model and reduced-integration elements (only one integration point). By using a finite element size corresponding to six elements through the thickness, see Section 4.1 and Fig. 4, the heterogeneity of the strain fields in the simulations was similar to those observed in the experiments. Henceforth, reduced-integration elements and an element size corresponding to six elements through the thickness are applied unless otherwise stated. Note that after the finite element type and size are set, fine-calibration of the model may be performed.
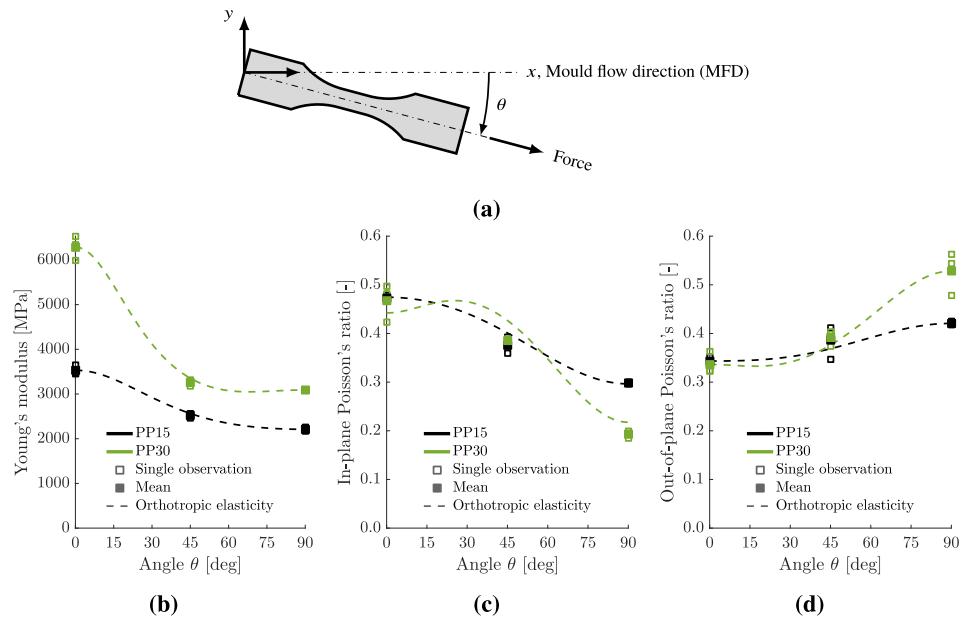
Fig. 3. (a) Definition of specimen orientation angle θ. Calibrated (analytical) orthotropic model demonstrated for: (b) Young's modulus and (c) in-plane and (d) out-of-plane Poisson's ratios.

Table 1
Calibrated engineering coefficients of the orthotropic elastic part of the model.

Material	E_1 [MPa]	E_2 [MPa]	E_3 [MPa]	ν_{12} [−]	ν_{23} [−]	ν_{31} [−]	G_{12} [MPa]	G_{23} [MPa]	G_{31} [MPa]
PP15	3531	2210	2871	0.47	0.42	0.28	915	734	734
PP30	6287	3090	4689	0.44	0.53	0.25	1175	865	865

Table 2
Calibrated parameters for the damage part of the model.

Material	E_0 [MPa]	a_f [−]	G_f [N/mm]	$\kappa_{0,\text{mean}}$ [−]	$\kappa_{0,\text{std}}$ [−]	$\kappa_{0,\text{min}}$ [−]
PP15	3531	2	7.5	0.0210	0.0190	0.0040
PP30	6287	2	7.5	0.0160	0.0170	0.0040

4. Validation against tensile tests

4.1. Setup, methods and numerical model

Quasi-static tensile tests of PP, PP15 and PP30 were performed at room temperature in a Zwick/Roell Z030 test machine (30 kN load cell) using specimens with the nominal geometry shown in Fig. 4a. The locations of the specimens in the injection-moulded plates are found in the supplementary material. Three replicate tests were carried out for each combination of material and angle. All tensile tests were performed at a crosshead velocity of 0.9 mm/min, which corresponds to measured strain rates around $1 \cdot 10^{-4}$ s^{-1}. Mechanical wedge grips were used to support the specimens and digital image correlation (DIC) measurements were obtained from two cameras with perpendicular view, one positioned directly in front of the specimen and one monitoring the through-thickness side (acquisition frequency 3 Hz). The DIC software *eCorr* (Fagerholt, 2019; Fagerholt et al., 2013) was applied to calculate the deformations, using a DIC mesh with element size of 25×25 pixels^2 (around 0.27×0.27 mm^2). The local coordinate system of a test, defined in Fig. 4a, is selected such that the x_1-axis is parallel to the force, the x_2-axis is along the in-plane
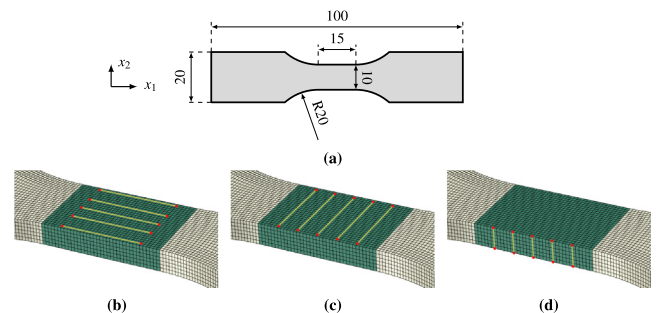

Fig. 4. (a) Geometry of tensile test specimen (dimensions given in mm) and the local coordinate system of a test. The yellow vectors defined by the red nodes form the basis for the applied strain measure in the (b) x_1-, (c) x_2- and (d) x_3-direction.

transverse direction of the specimen, while the x_3-axis is in the out-of-plane direction.

Representative normal strain measures ε_{11}, ε_{22} and ε_{33} in the three coordinate directions are computed as the mean logarithmic strain from five parallel vectors along the respective directions, as illustrated in Figs. 4b-d. The length of the longitudinal vectors is 2/3 of the gauge section length. True stress is calculated as

$$\sigma = \frac{F}{A} = \frac{F}{A_0 \exp(\varepsilon_{22} + \varepsilon_{33})} \tag{16}$$

where F is the force, A is the current area and A_0 is the initial area. Young's modulus, in-plane and out-of-plane Poisson's ratios and strain rate are calculated by linear regression of the relevant response curves in the interval between 10% and 30% of maximum force. The end of the experiments is defined by manually selecting the last data point on the global force–displacement curve before the final, uncontrolled load-drop.

The finite element model of the tensile test, shown in Fig. 2c, is based on the nominal specimen geometry (Fig. 4a), using thickness 2.73 mm (mean value of measured plate-thickness) and length 80.0 mm (accounts for the application points of the mechanical grips). The model is discretized with six elements through the thickness using eight-node linear brick elements with reduced integration and default hourglass control (C3D8R). To account for the stochastic effect of the drawn damage initiation (κ_0) values, five replicate simulations are run for each combination of material and orientation. Representative logarithmic strain measures and true stress are calculated exactly the same way as for the experi-
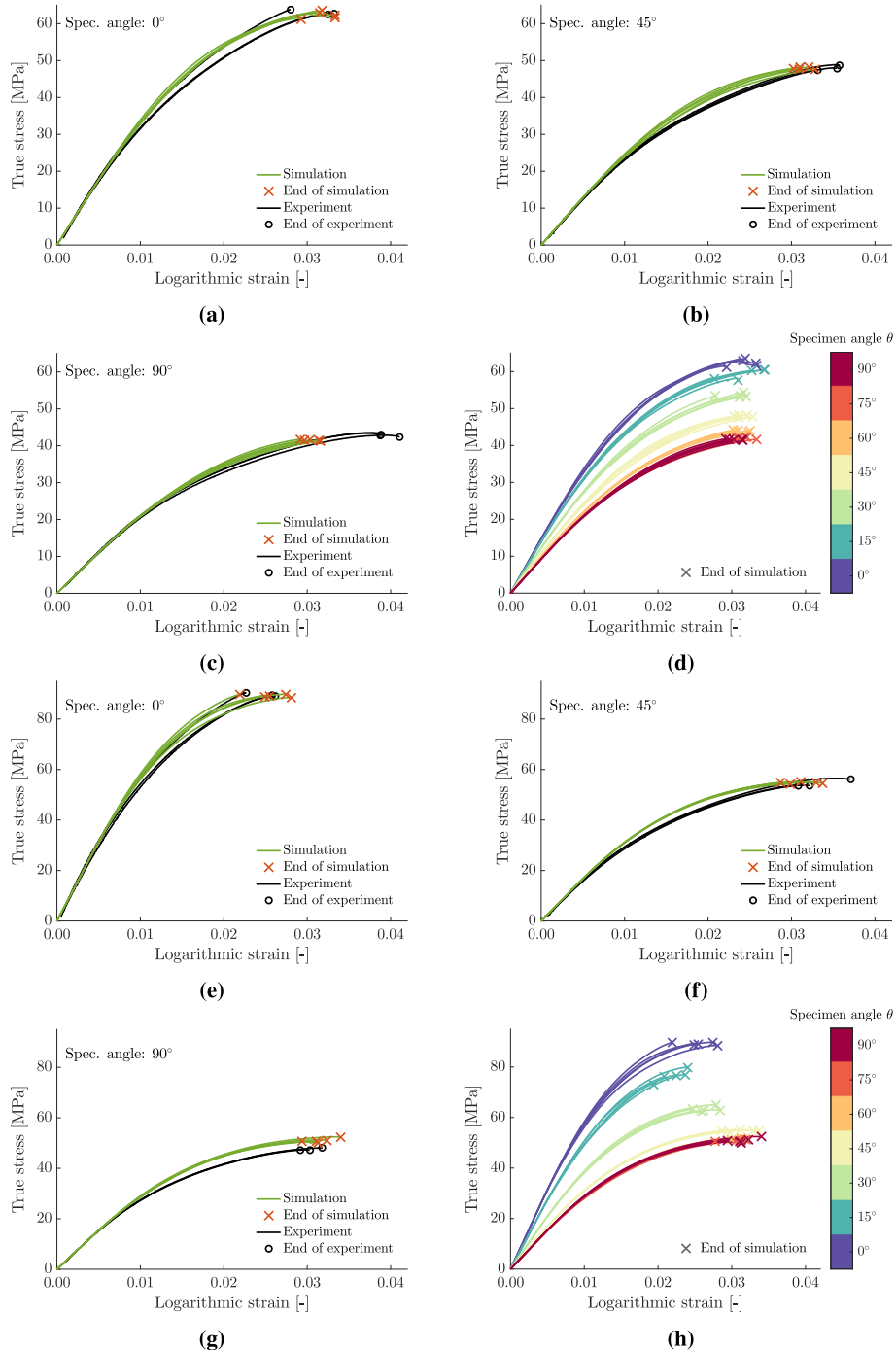

Fig. 5. Stress–strain curves from tensile test simulations and experiments: (a) 0° of PP15, (b) 45° of PP15, (c) 90° of PP15, (d) all simulations of PP15, (e) 0° of PP30, (f) 45° of PP30, (g) 90° of PP30 and (h) all simulations of PP30.

Petter Henrik Holmström, Arild Holm Clausen, T. Berstad et al.

International Journal of Solids and Structures 230–231 (2021) 111142

Table 3

Mean values of Young's modulus E, stress at maximum force $\sigma_{F_{max}}$, ultimate strain ε_{ult}, in-plane Poisson's ratio $v_{in-plane}$ and out-of-plane Poisson's ratio $v_{out-of-plane}$ from the tensile tests of PP, PP15 and PP30.

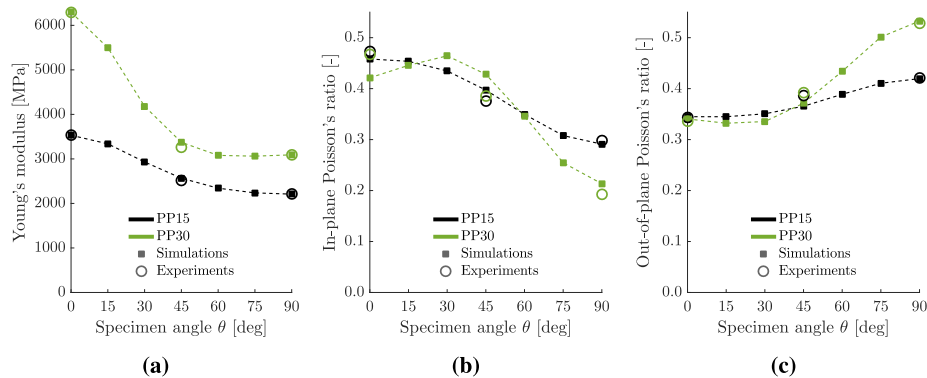| Material	θ [deg]	E [MPa]	$\sigma_{F_{max}}$ [MPa]	ε_{ult} [−]	$v_{in-plane}$ [−]	$v_{out-of-plane}$ [−]
PP	0	1562	35.5		0.41	
	45	1516	35.1		0.40	
	90	1559	35.5		0.39	
PP15	0	3531	63.0	0.032	0.47	0.34
	45	2518	48.1	0.035	0.38	0.39
	90	2210	43.3	0.040	0.30	0.42
PP30	0	6287	89.6	0.025	0.47	0.34
	45	3258	54.7	0.033	0.39	0.39
	90	3090	47.5	0.030	0.19	0.53

Fig. 6. Comparison of (a) Young's modulus and (b) in-plane and (c) out-of-plane Poisson's ratios from simulations and experiments.

ments, see Fig. 4 and Eq. (16). The end of the simulations is defined the same way as for the experiments, as explained above.

4.2. Results

The stress–strain curves from experiments and simulations are presented in Fig. 5. We observe a relatively short linear region followed by a gradual reduction of the secant modulus before a brittle fracture occurs. The strength and fracture strain for the 45°- and 90°-simulations are generally in good agreement with the experiments. This is indeed noticeable, since the damage part of the model was calibrated for the 0°-direction. For the 90° simulations of PP15, the model is able to predict the correct maximum stress level, but not the increased ductility observed in the 90° tests compared to 0° tests. While the tests were carried out in three directions (0°, 45° and 90°), simulations were performed in seven directions, also incorporating the 15°, 30°, 60° and 75° directions. The stress–strain curves from all numerical simulations on PP15 and PP30 are compiled in Fig. 5d and Fig. 5h, respectively.

Table 3 lists Young's modulus, stress at maximum force, ultimate strain and in-plane and out-of-plane Poisson's ratios from the experiments. Fig. 6 compares the elastic properties from the tests and simulations, using the very same procedure described in Section 4.1 to calculate the coefficients. Since the analytical orthotropic model was in close agreement with the experimental results in Fig. 3, it was expected that similar results can be extracted from simulations of the tensile tests.

As discussed in relation to Eq. (13), the regularization procedure is formulated such that the softening modulus decreases for material orientations with decreasing values of Young's modulus. A consequence of this is seen for PP30 in Fig. 5h, where the fracture strain is slightly larger for the specimen orientations with lowest stiffness ($\theta = 45°$ to $\theta = 90°$) than for the other directions. The

results demonstrate also that the magnitude of this effect is small unless the difference in Young's modulus in the 0°- and 90°-direction is large.

5. Discussion of model behaviour

In the following, the performance of the material model is demonstrated for some numerical test cases, using the tensile test in the 0° direction of PP30 as basis. The FE model presented in Section 4.1 is applied in the simulations and combined with material model parameters close to the calibrated parameters from Section 3.

5.1. Damage evolution

First, we will investigate how damage evolves for an FE model of a tensile test. Based on the probability density distribution in Fig. 7a, a κ_0-value is drawn for each element of the FE model. Fig. 7b plots the stress–strain curve from the tensile test simulation and Figs. 7c–h present contour plots of the damage parameter D at different deformation levels. Although not shown here, the early damaged elements in Fig. 7c correspond to the elements which have the lowest assigned κ_0-values. As the deformation level increases, two sources to new elements with non-zero damage are observed; elements with, relatively speaking, low κ_0-values and elements located in the proximity of already damaged elements. Step-by-step, the damaged regions coalesce, while some regions remain virtually undamaged. Note that the regions of high damage are spread over the gauge section, and there is no clear sign of where the final fracture will occur.

Fig. 8 presents the stress–strain curves from ten realizations of assigned κ_0-values, where the FE model draws κ_0 from exactly the same distribution for each simulation. The results show that the tangent modulus and the strength are very similar between the
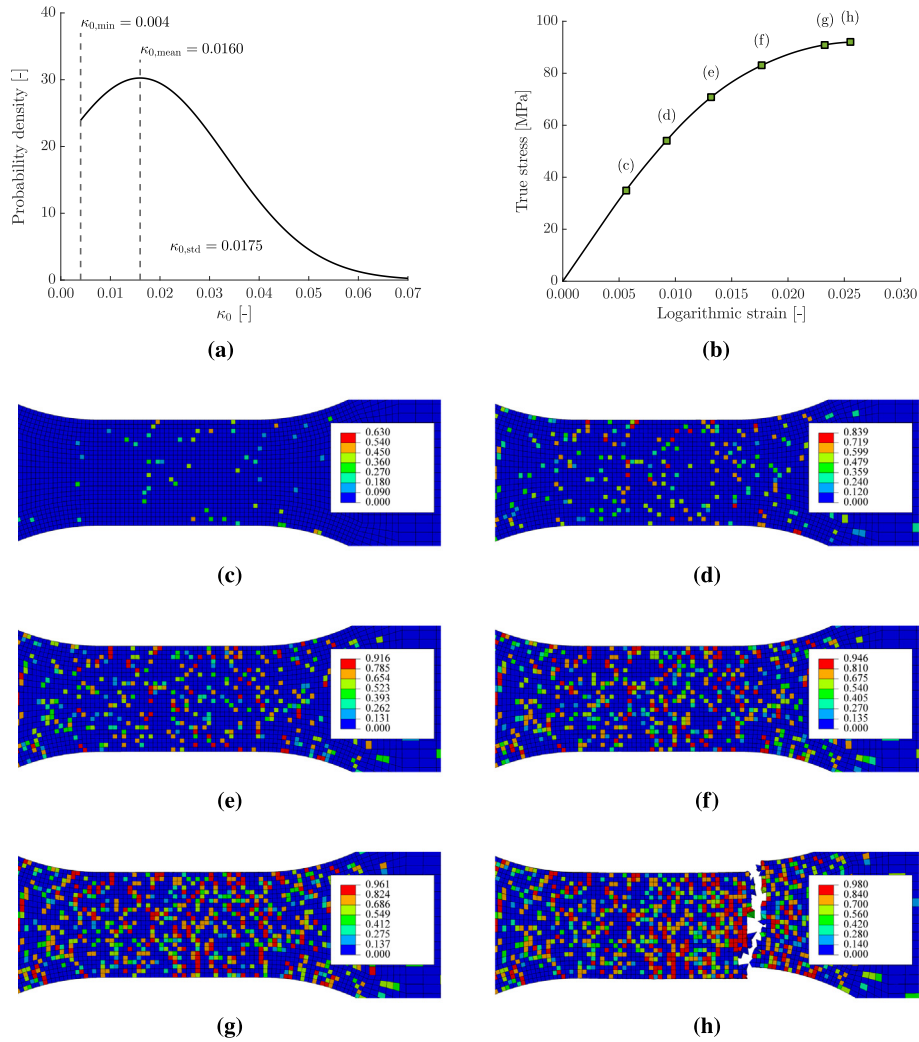
Petter Henrik Holmström, Arild Holm Clausen, T. Berstad et al.

International Journal of Solids and Structures 230–231 (2021) 111142

Fig. 7. (a) Applied distribution of the damage initiation parameter κ_0, (b) stress–strain curve of a tensile test simulation where (c), (d), (e), (f), (g) and (h) show values of the damage variable $D \in [0, 1)$ at the deformation levels indicated in (b).

ten numerical replicates, whereas the fracture strain is clearly affected by the actual realization of assigned κ_0-values.

5.2. Length scale effects and mesh sensitivity

The presented model has an intrinsic length scale defined by the length over which we assign the κ_0-values, where the most prag-
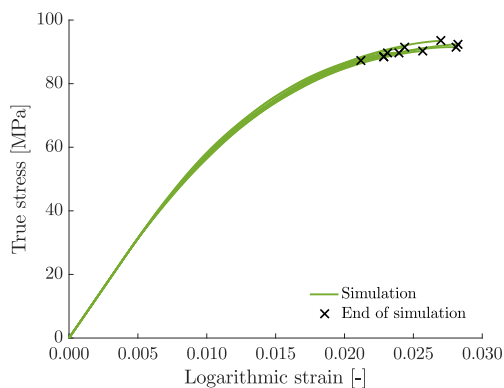
Fig. 8. Stress–strain curves for ten tensile test simulations, where the realization of the values of the damage initiation parameter κ_0 is unique for each simulation.

matic approach is simply to draw κ_0-values independently at each integration point of the finite elements. This requires no specific assignment procedure, which, conveniently, seems to be sufficient for practical usage of the model. For a numerical evaluation of the model, however, we need improved control, both to facilitate assignment of values over a different length scale than the size of the finite elements and to enable for assigning the exactly the same realization of values to different FE models. Inspired by Knoll (2015), the following procedure was established to control the assignment of κ_0-values:

1. An *assignment mesh* is generated as a rectangular cuboid with a structured grid. For each element in the assignment mesh, a unique κ_0-value is drawn from the truncated distribution in Eq. (15).
2. The finite element model is then completely submerged into the assignment mesh, as illustrated in Fig. 9. For each finite element, all integration points inherit the κ_0-value of the assignment mesh at the location of the centroid of the finite element.

The assignment procedure defines the length scale of the heterogeneities by the element size of the assignment mesh instead of the FE mesh. This opens for mesh sensitivity studies of the material model. To do this, three otherwise identical FE models of the
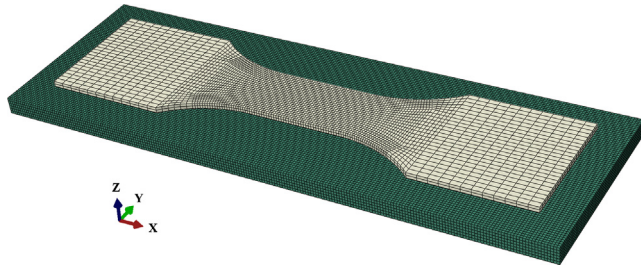
Fig. 9. Illustration of the procedure used to assign values of the damage initiation parameter κ_0 to the elements in the FE model. The here partly submerged FE model (beige) is completely submerged in the assignment mesh (green) in applications of the procedure.

tensile test specimen are established and discretized with element sizes corresponding to 6, 12 and 24 elements through the thickness. Next, κ_0-values are assigned to the three FE models from the very same realization of an assignment mesh with element size corresponding to 6 elements through the thickness, as

demonstrated in Figs. 10a, c and e. Hence, except for the finite element size, the three FE models are identical. Fig. 10g plots the stress–strain curves from the simulations. It appears that the ultimate stress and fracture strain are slightly reduced with the element size, but the effect is small if one considers the large difference in element size. Figs. 10b, d and f show contour plots of the logarithmic normal strain ε_{11} in the longitudinal direction at approximately the same global deformation level, indicated by markers in Fig. 10g. We observe remarkable similarities between the three displayed strain fields and it is clear that the initially assigned κ_0-values are crucial for the evolution of the deformation fields. As expected, the peak strain in the local regions increases for decreasing finite element size because larger elements smooth the local variations. To conclude, the presented results demonstrate that the applied regularization procedure (see Eq. (13)) works as intended and the mesh sensitivity of the material model is rather low.

To investigate what happens if we change the length scale of the heterogeneities while keeping the finite element size fixed, κ_0-values are assigned to the FE model with 12 elements through the thickness from assignment meshes with 6 and 12 elements
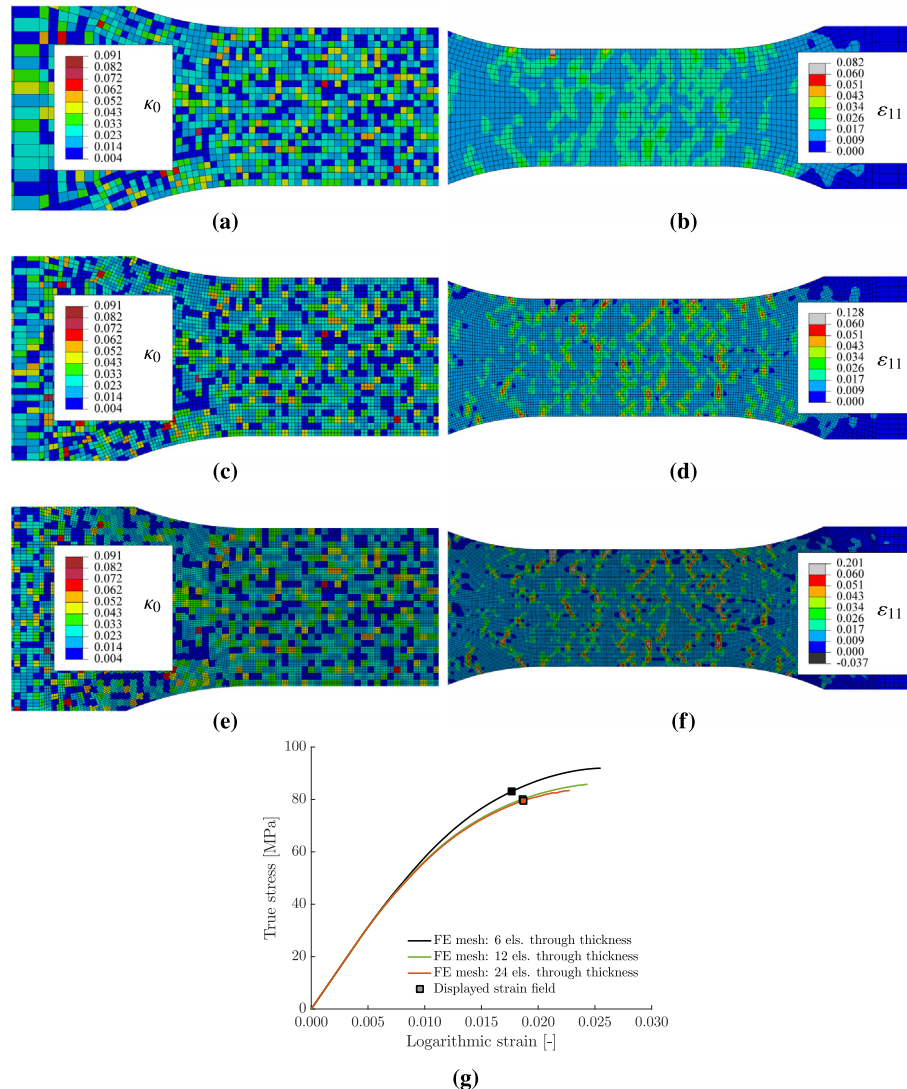

Fig. 10. Damage initiation (κ_0) values for FE models of the tensile test, with (a) 6, (c) 12 and (e) 24 elements through the thickness. The κ_0-values are assigned from exactly the same realization of an assignment mesh with 6 elements through the thickness. Contour plots of logarithmic normal strain ε_{11} in the longitudinal direction are shown for the FE models with (b) 6, (d) 12 and (f) 24 elements through the thickness at the deformation levels indicated in the stress–strain curves in (g). The negative value in the lower bound of (f) is caused by compressive strains in elements adjacent to already eroded elements.

through the thickness, as demonstrated in Fig. 10c and Fig. 11a, respectively. The two FE models are identical, except for the length scale over which we assign the κ_0-values and obviously the realization of the κ_0-values. Fig. 11c plots the stress–strain curves from the two simulations, and we observe that both the strength and fracture strain are lower when we distribute the κ_0-values over a larger length scale. A similar observation was reported by Su et al. (2010). Fig. 10d and Fig. 11b show the strain fields at approximately the same level of global deformation, indicated by markers in Fig. 11c. The strain fields become more heterogeneous when we assign κ_0-vales over a larger length scale, the local regions of large strains are both physically larger and have higher peak values. This probably also explains the reduced strength and ductility seen in Fig. 11c. The results demonstrate that the length scale of the heterogeneities is not arbitrary and should be taken into consideration.

5.3. Sensitivity of model parameters

We will now consider the sensitivity of some of the model parameters. Assuming that the material stiffness ($E = E_0$), the damage initiation parameter (κ_0) and the finite element size (h_{el}) are

already determined, the fracture energy parameter G_f governs the softening slope and thereby the area under the stress–strain curve according to Eq. (13). The effect of G_f is demonstrated by running tensile test simulations for the six different G_f-values presented in Fig. 12. A slightly modified κ_0-distribution compared to Fig. 7a is applied in the simulations ($\kappa_{0,\min} = 0.004$, $\kappa_{0,\mean} = 0.020$ and $\kappa_{0,\std} = 0.0075$). The assignment procedure is used to assign exactly the same realization of κ_0-values, such that the starting points for the simulations indeed are identical. Fig. 12 presents the stress–strain curves from the simulations. One interpretation of the results is that a master stress–strain curve exists for a large G_f-value, and reducing the G_f-value leads to prediction of fracture for a lower strain along that master curve. Hence, G_f is an effective variable for controlling the ductility of the material.

Next, the effect of the mean value of the κ_0-distribution, $\kappa_{0,\mean}$, is demonstrated by running tensile test simulations where all other material model parameters are fixed. Fig. 13a plots the applied distributions together with the stress–strain curves from the tensile tests in the 0°-direction of PP30 (Fig. 5e). As a digression, the reader may note that the lower bound $\kappa_{0,\min}$ is set to a value which corresponds to the end of the linear part of the experimental stress–strain curve. Fig. 13b presents the results from the simulations,
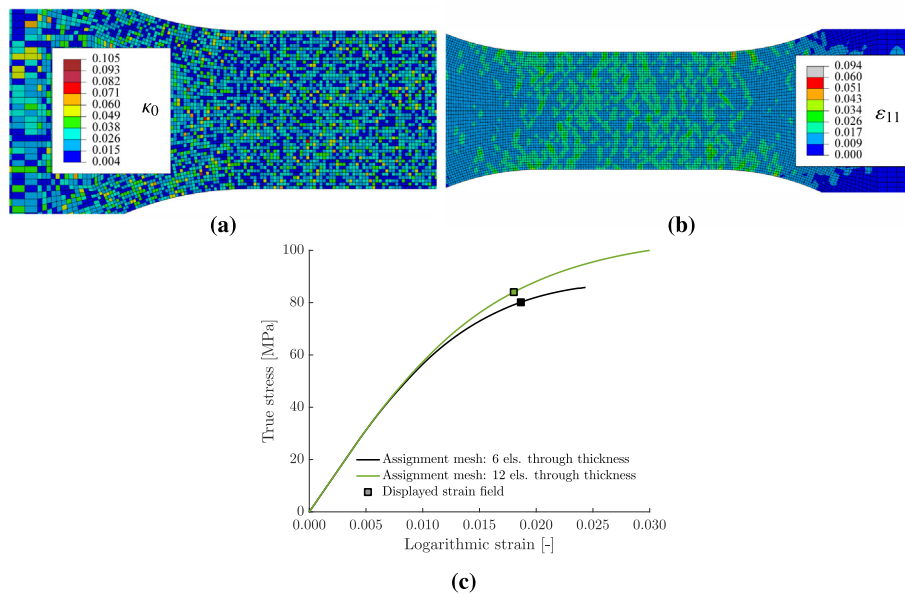

Fig. 11. (a) Damage initiation (κ_0) values for an FE model of the tensile test with 12 elements through the thickness, assigned from an assignment mesh with 12 elements through the thickness. (b) Contour plot of logarithmic strain in the longitudinal direction for the same FE model. (c) Stress–strain curves from tensile test simulations with 12 elements through the thickness and two different assignment mesh sizes.
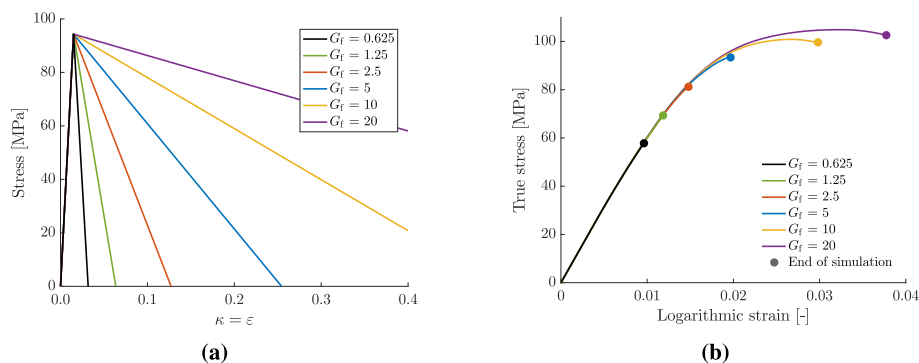

Fig. 12. (a) Model behaviour in a given material direction for different values of the fracture energy parameter G_f. (b) Stress–strain curves from tensile test simulations in one material direction and different values of the fracture energy parameter G_f.
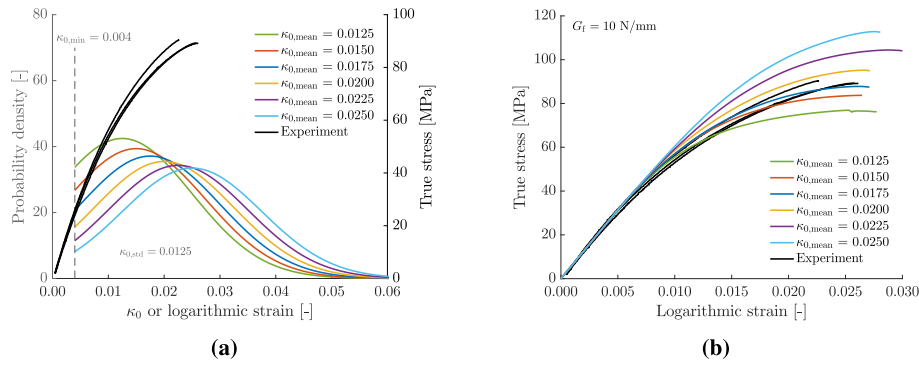
Petter Henrik Holmström, Arild Holm Clausen, T. Berstad et al.

International Journal of Solids and Structures 230–231 (2021) 111142

Fig. 13. (a) Distribution for the damage initiation parameter κ_0 (left vertical axis) and stress–strain curves from tensile tests of PP30 (right vertical axis). (b) Stress–strain curves from tensile test simulations for different values of $\kappa_{0,\mathrm{mean}}$.

and we observe, as expected, that the maximum stress increases for increasing values of $\kappa_{0,\mathrm{mean}}$. The tangent modulus depends strongly on the shape of the κ_0-distribution, particularly in the region near the lower bound $\kappa_{0,\mathrm{min}}$. Unless the value of the probability density function is rather large in this region, the tangent modulus tends to be overestimated. This is demonstrated in Fig. 13b, where the largest tangent modulus is observed for the simulation with the lowest value of the probability density at the left-truncation $\kappa_{0,\mathrm{min}}$, and vice versa. A general observation from these and additional simulations not included for brevity is that the effect of $\kappa_{0,\mathrm{mean}}$ on the ultimate strain is small.

6. Validation against other tests

Section 4.2 demonstrated that the model captures the stress–strain curves from the tensile tests. Recall that data from all three tensile directions 0°, 45° and 90° were applied to calibrate the orthotropic elastic part of the model, while the damage part of the model is solely based on information from the 0° tests. As a further validation of the model, numerical predictions will now be compared with experimental results from open-hole tensile tests and three-point bending tests. By this, the model is challenged to deal with other stress states than uniaxial tension. The open-hole tensile tests and three-point bending tests were carried out in the same test machine and monitored by the same camera as the tensile tests, see Section 4.1.

6.1. Open-hole tensile tests

Quasi-static open-hole tensile tests were performed for 0°-specimens of PP15 and PP30, using the specimen geometry illustrated in Fig. 14a. Mechanical wedge grips were used to support the specimens and DIC measurements were obtained from one camera placed directly in front of the specimens. The deformation measure used in the open-hole tensile tests is the nominal strain of a 25.0 mm long vector, illustrated in Fig. 14b, which is defined by the nodes at the edges of the DIC mesh. It is, however, not straightforward to generate a DIC-mesh of exact dimensions defined in millimeters. The following procedure was applied to ensure high accuracy:
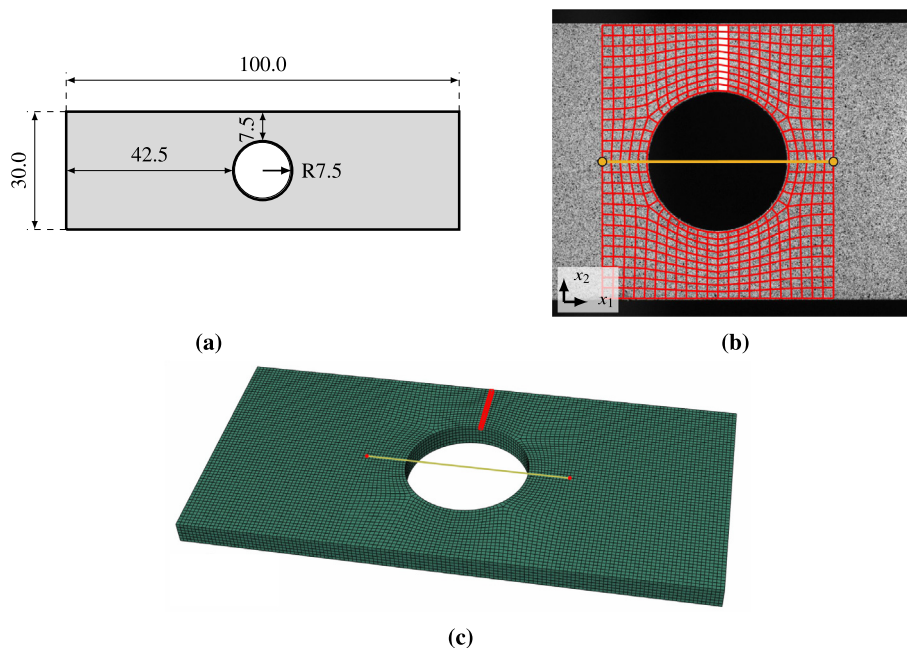

Fig. 14. Open-hole tensile test setup. (a) Geometry of the test specimen (dimensions given in mm). (b) Applied DIC mesh (in red) with 25.0 mm long vector used as strain measure (in orange) and selected elements used for strain analysis (highlighted in white). (c) FE model of the test.

Petter Henrik Holmström, Arild Holm Clausen, T. Berstad et al.

International Journal of Solids and Structures 230–231 (2021) 111142

1. A first mesh (similar to Fig. 14b) was generated in Abaqus CAE, with longitudinal dimension 25.0 mm and otherwise nominal values (30.0 mm in the transverse direction and 15.0 mm hole diameter).
2. A second mesh with longitudinal dimension 25.0 mm was generated, now with 0.2 mm gap to each specimen edge.
3. The first mesh was imported to the DIC software and scaled such that the mesh fitted perfectly to the undeformed specimen.
4. The second mesh was also imported to the DIC software and scaled such that the longitudinal dimension (25.0 mm) was exactly the same as the already scaled first mesh.

By this procedure, the second mesh is correctly scaled and has sufficient gaps to the specimen edges to avoid instabilities in the correlation process. The approximate element size of the mesh is 44×68 pixels^2 near the hole (around 0.71×1.10 mm^2). The crosshead velocity was 0.18 mm/min for two replicates and 1.80 mm/min for the third one. A representative strain rate value was computed as the mean elastic strain rate of the elements highlighted in Fig. 14b and the results showed that the test at 1.80 mm/min induced a comparable, but slightly higher, strain rate than the rate observed in the tensile tests.

Fig. 14c presents the finite element model of the open-hole tensile test, which is based on the nominal geometry from Fig. 14a and the measured mean plate thickness of 2.73 mm. By setting the length of the FE model to 63 mm, the boundary conditions are enforced at approximately the same locations as the mechanical grips in the experiments. The FE model applies the same element formulation and approximately the same element size, six elements through the thickness, as used in the FE model of the tensile test. The representative deformation measure, illustrated by the yellow vector in Fig. 14c, is extracted exactly the same way as explained for the experiments (see Fig. 14b).

Fig. 15 plots the force-strain curves from the experiments and simulations of the open-hole tensile test. For both materials, the results from the simulations correspond well to the experimental result for crosshead velocity 1.80 mm/min, having a strain rate close to that of the tensile tests used for calibration of the model. It is noticeable that not only the stiffness and tangent modulus is well predicted, but also the maximum force and the fracture strain. Another observation from the test results reported in Fig. 15 is that the stiffness and strength increase with strain rate. The material model does not include any viscous effects, and it is therefore not able to capture the response in the tests carried out at the slow rate of 0.18 mm/s. Modelling of viscoelasticity is outside the scope of this work, but could be incorporated in an augmentation of the model. Nevertheless, Fig. 15 illustrates the magnitude of the strain-rate effect for the fibre-reinforced PP material at hand, and the pos-

sible corresponding error associated with the pragmatic modelling approach presented herein.

The local response in the part of the model experiencing the largest strains is addressed in Fig. 16, again comparing experimental and numerical results. Fig. 16b shows the strains of a row of elements near the hole, highlighted in Fig. 14b and Fig. 14c, for the simulations and a PP15 test for the strain levels A, B and C indicated in Fig. 16a. The normalized coordinate system defined in Fig. 16b, where 0.0 corresponds to the upper specimen edge and 1.0 corresponds to the edge of the hole, is applied for the initial x_2-coordinate of the element centres. The corresponding values of the element strain ε_{11} are extracted from the simulations, where the mean value from the five replicate simulations is used at each element location and deformation level. The experimental results demonstrate, as expected, that the element strains increase drastically as the distance to the hole decreases, a tendency which is pronounced with the global deformation level. The simulations coincide with the experiments far from the hole, but the simulations predict significantly larger local strains near the hole than observed in the experiments, despite that the global force-strain curves are well captured. One possible explanation for this is that smaller elements are applied near the hole in the numerical simulations than in the DIC mesh used to determine the strain field in the experiments.

6.2. Three-point bending tests

Quasi-static three-point bending tests at a crosshead velocity of 9.0 mm/min were performed for 0°- and 90°-specimens of PP15 and PP30, using the specimen geometry illustrated in Fig. 17a. As a reference, experiments were also performed for the unreinforced polypropylene material. The dimensions of the specimen were selected such that the width was approximately ten times the thickness, which is supposed to ensure nearly plane strain conditions (Yu and Shang, 1996). Fig. 17b illustrates the test setup and Fig. 17c shows an image of the test rig with an assembled specimen. DIC was applied to measure strains on the through-thickness side of the specimens using a mesh of seven elements through the thickness, as demonstrated in Fig. 17d. The DIC element size is 69×69 pixels^2 (around 0.37×0.37 mm^2). The applied representative displacement measure is the mean vertical displacement of the nodes highlighted in Fig. 17d, a measure which coincides with the crosshead displacement from the test machine. The elastic strain rate on the tensile side of the experiments was around 9×10^{-4} s^{-1}, obtained by computing the mean strain rate of the eight centred elements of the bottom row of the mesh in Fig. 17d. Hence, the elastic strain rates observed in the bending tests range from zero (at the neutral axis) to one decade higher than the measured strain rate from the tensile tests.
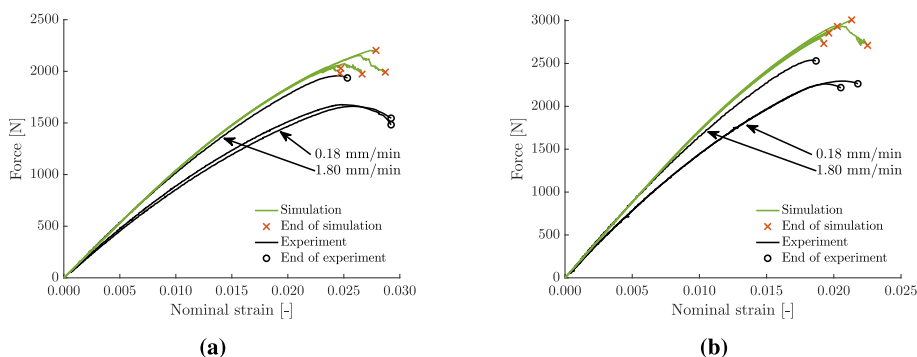

Fig. 15. Open-hole tensile tests: force-strain curves from simulations and experiments for (a) PP15 and (b) PP30.
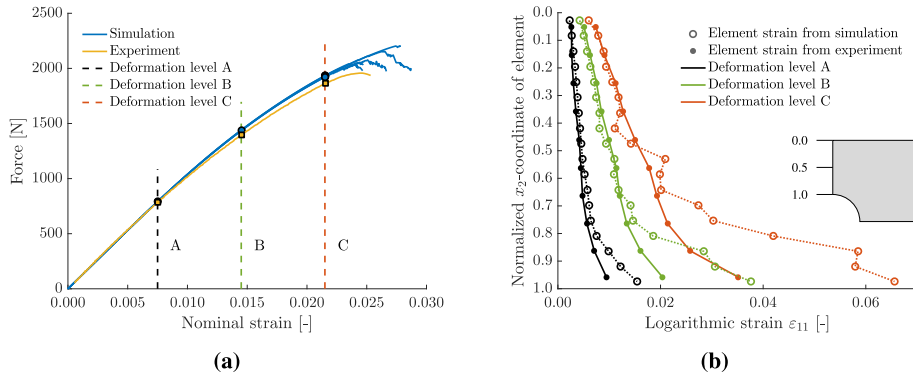
Fig. 16. Open-hole tensile tests: (a) Stress–strain curves from simulations and a representative PP15 test. (b) Element strain components ε_{11} shown at the deformation levels indicated in (a). The considered elements from the FE model and the experiment are highlighted in Fig. 14b and Fig. 14c, respectively.
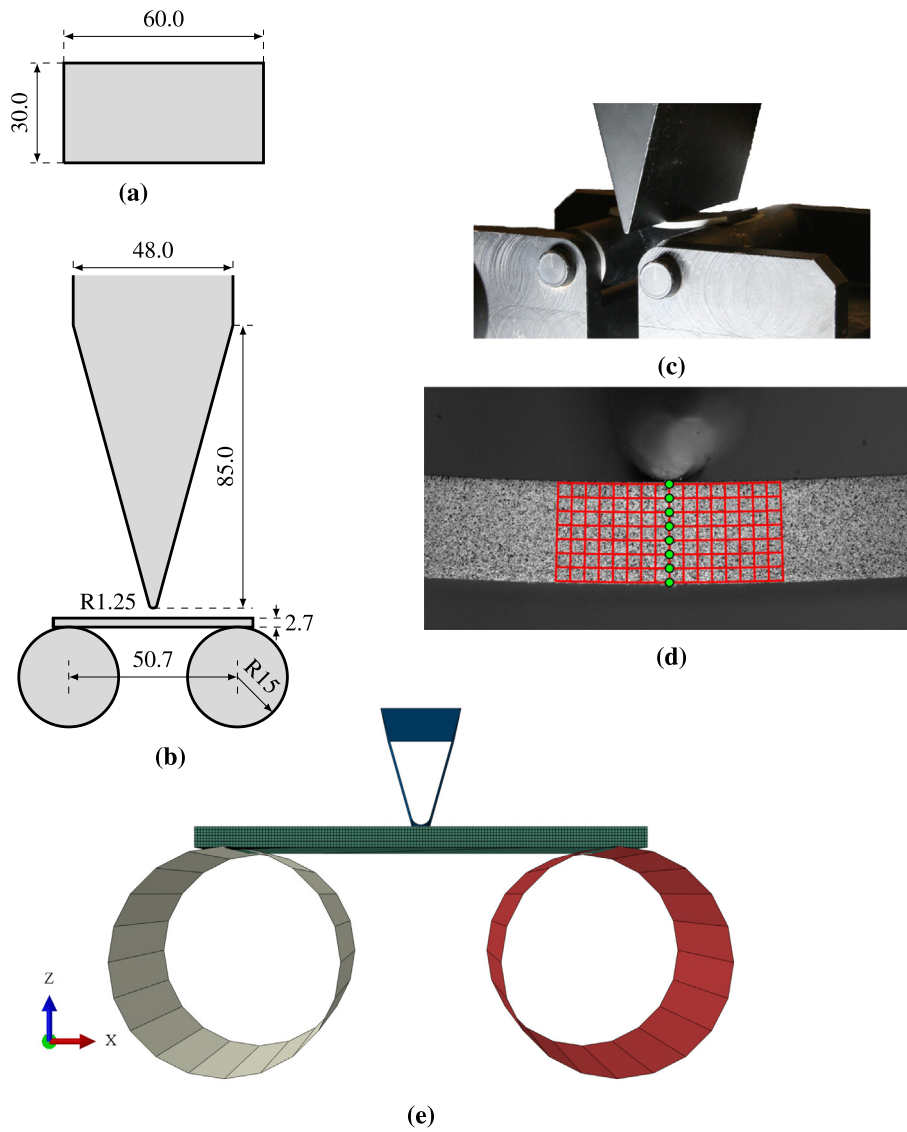

Fig. 17. Three-point bending test setup. (a) Top and (b) side view of the test setup (dimensions given in mm). (c) Image of the test setup. (d) Camera view, the DIC-mesh (red) and the nodes used as displacement measure (green). (e) FE model of the test.

An FE model of the three-point bending test is presented in Fig. 17e. The nominal geometry combined with the measured mean plate thickness of 2.73 mm is used for the deformable spec-imen (green), whereas *analytical rigid* parts are applied for the bending punch (blue) and supports (beige and red). Surface-to-surface contact with finite sliding is applied, using a penalty for-

mulation for the tangential behaviour and "hard" contact for the normal behaviour. Rather small differences were seen in simulation results for friction coefficients of 0.1 and 0.5, and henceforth, the value of 0.1 is applied in all presented simulations. To facilitate comparison of results, the same discretization as used in the DIC analysis of the experiments, i.e. seven elements through the thickness, is applied in the FE model. The displacement measure in the simulations is the vertical displacement of the rigid bending punch.

Figs. 18a and b present the force–displacement curves from the three-point bending experiments and simulations. The stiffness, strength and fracture are generally well captured for PP15, except for a slight underestimation of the fracture strain in the 90°-direction. For the 0°-direction of PP30, we observe that the predicted stiffness corresponds to the experiments, while the strength and fracture strain are slightly overestimated. For the 90°-direction of PP30, the stiffness and strength are overestimated while the fracture strain is underestimated. Two possible explanations for the discrepancies in the results for the 90°-direction of PP30 are outlined in the following. Firstly, for a 90° bending specimen, the

majority of fibres oriented in the stress direction are located in the central region (the *core*) in the through-thickness direction (Bernasconi et al., 2007; Rolland et al., 2016; Hessman et al., 2019; Holmström et al., 2020). Here, the strain and thereby the fibre stress is negligible. This makes the 90° bending stiffness lower than the corresponding 90° tensile stiffness, which is used in the elastic part of the material model. Zhu et al. (2020) report a similar result. The reinforcing effect of the fibres is indeed limited in this deformation mode, and from the figures we may observe that the 90° bending stiffness of PP15 and PP30 is just slightly above the corresponding value for the unreinforced PP. Secondly, for 90° bending specimens, the majority of the fibres in the highly loaded shell layers is oriented transverse to the load, which promotes the debonding failure mechanism on the tensile side of the plate (Rolland et al., 2016; Rolland et al., 2017; Nouri et al., 2017). This is different from the calibration experiment for the damage model, namely the 0° tensile test, where fibre pullout and fibre fracture are the primary failure mechanisms (Rolland et al., 2016; Rolland et al., 2017; Nouri et al., 2017). PP15 has a much less pronounced variation of fibre orientations through the thickness compared to
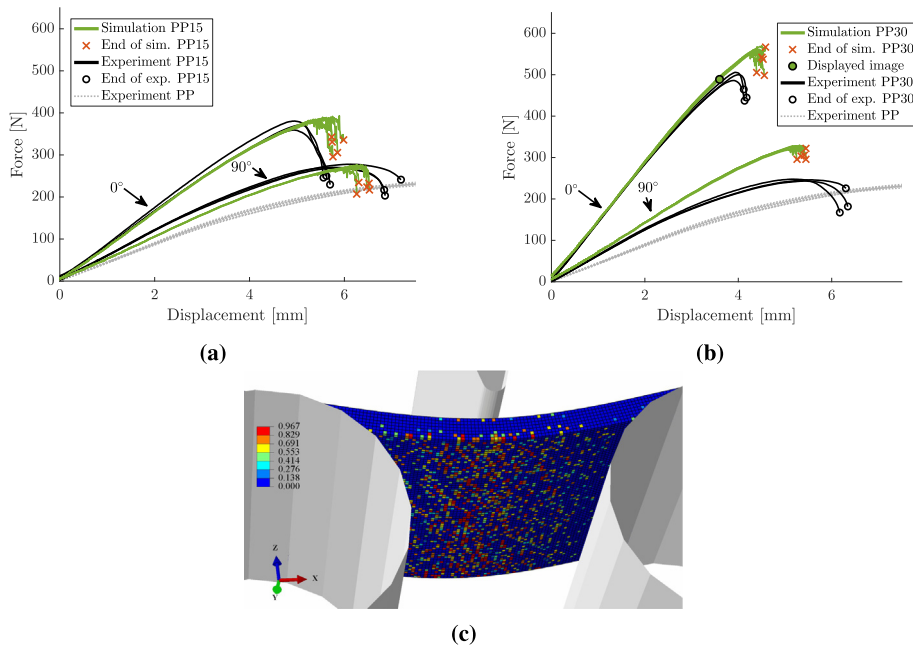

Fig. 18. Three-point bending tests: force–displacement curves from simulations and experiments for (a) PP15 and (b) PP30. (c) Element values of the damage variable $D \in [0, 1)$ from a PP30 simulation at the deformation level indicated in (b).
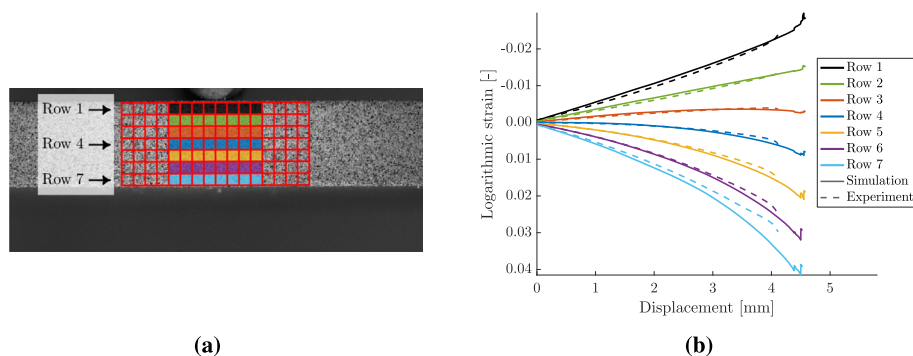

Fig. 19. Through-thickness strain analysis of a representative 0°-direction three-point bending tests of PP30. (a) Numbering of element rows and (b) mean strain of the element rows from the simulations and the experiment.

Petter Henrik Holmström, Arild Holm Clausen, T. Berstad et al.

International Journal of Solids and Structures 230–231 (2021) 111142

PP30, which explains why the discussed features are less relevant for this material. Finally, Fig. 18c demonstrates how damage evolves in a three-point bending simulation of PP30. We observe that the values of the damage parameter $D \in [0, 1)$ approach 1 for a large number of elements at the given deformation level, indicated in Fig. 18b.

The through-thickness variation of longitudinal strain in the elements close to the punch from the simulations is now compared to one representative $0°$ three-point bending test of PP30. For each element row in Fig. 19a, Fig. 19b plots the mean strain of the eight highlighted elements, where an average measure is used to combine the results from the five replicate simulations. The correspondence between the simulation results and the experiment is excellent. Slightly larger strains are, however, seen on the tensile side of the plate (Row 7) in the simulations compared to in the experiments, similar to observations from the open-hole tensile tests (see Fig. 16). Note also that tensile strains develop in Row 4 (in the centre of the specimen), which is caused by damage evolution on the tensile side and a corresponding shift of the position of the neutral axis towards the compression side of the specimen.

7. Perspectives

Reducing costs and development time while simultaneously preserving, or even increasing, the flexibility, accuracy and reliability in the design process is an ambitious, but yet approachable objective for engineers today. In this regard, appropriate use of micromechanical material models and RVE (representative volume element) simulations may efficiently support calibration of macroscopic anisotropic material models and reduce the number of required experiments significantly. For fibre-reinforced polymers, one such example is the micromechanical material model proposed by Notta-Cuvier et al. (2013), which may be applied to replace the physical tensile tests in the $0°$, $45°$ and $90°$ direction by virtual tests (FE simulations). This micromechanical model defines the composite material behaviour by the matrix response, which may be determined in advance, the fibre volume content, usually known, and the fibre orientation distribution, which may be measured or possibly estimated from mould flow simulations. Similar computational approaches may reduce the number of physical experiments and speed up the calibration process significantly also for other materials. For instance, the macroscopic material model presented in this paper could possibly be calibrated from the computational approach for prepreg platelet molded composites (PPMCs) presented by Sommer et al. (2020). The model presented herein could also be used in combination with results from mould flow simulations (similar to e.g. Amiri-Rad et al., 2020). Assuming that a representative material behaviour exists, the material model could first be calibrated to this representative behaviour and then, to mimic the spatial variation of fibre orientations, the principal axes of the orthotropic material could be related to results from mould flow simulations throughout the part.

8. Conclusions

We have presented a computationally efficient progressive damage model, where an orthotropic elastic model is combined with linear softening, stochastic values of the damage initiation strain, and scalar damage variable. The model's performance is investigated both from a numerical point of view and validated against tensile tests ($0°$, $45°$ and $90°$), open-hole tensile tests ($0°$) and three-point bending ($0°$ and $90°$) tests of fibre-reinforced polypropylene with 15 wt.% (PP15) and 30 wt.% (PP30) glass fibres.

The main findings include:

- Although the material stress–strain curve is bi-linear for each integration point, the global stress–strain curve becomes highly non-linear due to the spatially heterogeneous damage initiation strains. Damage is first initiated in integration points with low damage initiation strain and tends to grow in the proximity of already damaged integration points such that a strongly heterogeneous strain field develops, as observed in experiments. The unique realization of the spatially heterogeneous material properties primarily affects the fracture strain, whereas little scatter is seen for the tangent modulus and strength. Fracture occurs shortly after the maximum force is reached and the model predicts a similar fracture strain for all material orientations. A regularization procedure ensures that the mesh sensitivity of the model is low.

- The model captures the anisotropic elastic behaviour, the tangent modulus and the fracture strain observed in the experiments. Correspondence between simulations and experiments is also obtained for the strength in the tensile tests, while the maximum force is slightly overestimated for open-hole and three-point bending tests for the PP30 material. Local strains near the hole in open-hole tests and on the tensile side of the three-point bending tests are larger in the simulations than in experiments.

The model is computationally efficient and easy to calibrate. By taking advantage of micromechanical models or representative volume element simulations, an efficient calibration procedure may be established for the presented macroscopic material model.

Declaration of Competing Interest

The authors declare that they have no known competing financial interests or personal relationships that could have appeared to influence the work reported in this paper.

Acknowledgements

Appendix A. Supplementary data

Supplementary data to this article can be found online at https://doi.org/10.1016/j.ijsolstr.2021.111142.

References

Abaqus 6.14, Online Documentation, Dassault Systèmes, 2014.

Amiri-Rad, A., Wismans, M., Pastukhov, L.V., Govaert, L.E., van Dommelen, J.A.W., 2020. Constitutive modeling of injection-molded short-fiber composites: Characterization and model application, J. Appl. Polymer Sci. e49248. https://doi.org/10.1002/app.49248.

Ayadi, A., Nouri, H., Guessasma, S., Roger, F., 2016. Determination of orthotropic properties of glass fibre reinforced thermoplastics using X-ray tomography and multiscale finite element computation. Compos. Struct. 136, 635–649. https://doi.org/10.1016/j.compstruct.2015.10.041.

Bažant, Z.P., Oh, B.H., 1983. Crack band theory for fracture of concrete. Matériaux et Constructions 16 (3), 155–177. https://doi.org/10.1007/BF02486267.

Bernasconi, A., Davoli, P., Basile, A., Filippi, A., 2007. Effect of fibre orientation on the fatigue behaviour of a short glass fibre reinforced polyamide-6. Int. J. Fatigue 29, 199–208. https://doi.org/10.1016/j.ijfatigue.2006.04.001.

de Borst, R., Verhoosel, C.V., 2017. Damage, Material Instabilities, and Failure, in: Encyclopedia of Computational Mechanics Second Edition, John Wiley & Sons Ltd, Chichester, UK, 2017, pp. 1–50. https://doi.org/10.1002/9781119176817.ecm2035.

De Monte, M., Moosbrugger, E., Quaresimin, M., 2010. Influence of temperature and thickness on the off-axis behaviour of short glass fibre reinforced polyamide 6.6 - Quasi-static loading, Composites Part A: Applied Science and Manufacturing 41 (7) (2010) 859–871. https://doi.org/10.1016/j.compositesa.2010.02.018.

Petter Henrik Holmström, Arild Holm Clausen, T. Berstad et al.

International Journal of Solids and Structures 230–231 (2021) 111142

Despringre, N., Chemisky, Y., Bonnay, K., Meraghni, F., 2016. Micromechanical modeling of damage and load transfer in particulate composites with partially debonded interface. Compos. Struct. 155, 77–88. https://doi.org/10.1016/j.compstruct.2016.06.075.

Desrumaux, F., Meraghni, F., Benzeggagh, M.L., 2001. Generalised Mori-Tanaka Scheme to Model Anisotropic Damage Using Numerical Eshelby Tensor. J. Compos. Mater. 35 (7), 603–624. https://doi.org/10.1177/002199801772662091.

Fagerholt, E., 2019. User manual - eCorr - Digital Image Correlation Tool. https://www.ntnu.edu/kt/ecorr.

Fagerholt, E., Børvik, T., Hopperstad, O.S., 2013. Measuring discontinuous displacement fields in cracked specimens using digital image correlation with mesh adaptation and crack-path optimization. Opt. Lasers Eng. 51 (3), 299–310. https://doi.org/10.1016/j.optlaseng.2012.09.010.

Gu, J., Li, K., Su, L., 2019. A Continuum Damage Model for Intralaminar Progressive Failure Analysis of CFRP Laminates Based on the Modified Puck's Theory. Materials 12 (20), 3292. https://doi.org/10.3390/ma12203292.

Hashin, Z., 1980. Failure Criteria for Unidirectional Fiber Composites. J. Appl. Mech. 47 (2), 329. https://doi.org/10.1115/1.3153664.

Hessman, P.A., Riedel, T., Welschinger, F., Hornberger, K., Böhlke, T., 2019. Microstructural analysis of short glass fiber reinforced thermoplastics based on x-ray micro-computed tomography. Compos. Sci. Technol. 183, 107752. https://doi.org/10.1016/j.compscitech.2019.107752.

Holmström, P.H., 2019. An experimental and numerical study of the mechanical behaviour of short glass-fibre reinforced thermoplastics, Ph.D. thesis, Norwegian University of Science and Technology, https://hdl.handle.net/11250/2763360.

Holmström, P.H., Hopperstad, O.S., Clausen, A.H., 2020. Anisotropic tensile behaviour of short glass-fibre reinforced polyamide-6. Compos. Part C: Open Access 2,. https://doi.org/10.1016/j.jcomc.2020.100019 100019.

Irgens, F., 2008. Continuum Mechanics. Springer.

Jendli, Z., Meraghni, F., Fitoussi, J., Baptiste, D., 2009. Multi-scales modelling of dynamic behaviour for discontinuous fibre SMC composites. Compos. Sci. Technol. 69 (1), 97–103. https://doi.org/10.1016/j.compscitech.2007.10.047.

Knoll, O., 2015. A probabilistic Approach in Failure Modelling of Aluminium High Pressure Die-Castings, Ph.D. thesis, Norwegian University of Science and Technology.

Kumar, R.S., Mordasky, M., Ojard, G., Yuan, Z., Fish, J., 2019. Notch-strength prediction of ceramic matrix composites using multi-scale continuum damage model. Materialia 6,. https://doi.org/10.1016/j.mtla.2019.100267 100267.

Lapczyk, I., Hurtado, J.A., 2007. Progressive damage modeling in fiber-reinforced materials. Compos. Part A: Appl. Sci. Manuf. 38 (11), 2333–2341. https://doi.org/10.1016/j.compositesa.2007.01.017.

Le, J.-L., Eliáš, J., 2016. A Probabilistic Crack Band Model for Quasibrittle Fracture. J. Appl. Mech. 83 (5), 1–7. https://doi.org/10.1115/1.4032692.

Ly, H.-B., Desceliers, C., Minh Le, L., Le, T.-T., Thai Pham, B., Nguyen-Ngoc, L., Doan, V. T., Le, M., 2019. Quantification of Uncertainties on the Critical Buckling Load of Columns under Axial Compression with Uncertain Random Materials. Materials 12 (11), 1828. https://doi.org/10.3390/ma12111828.

Maimí, P., Camanho, P.P., Mayugo, J.A., Dávila, C.G., 2007. A continuum damage model for composite laminates: Part I - Constitutive model. Mech. Mater. 39 (10), 897–908. https://doi.org/10.1016/j.mechmat.2007.03.005.

Maimí, P., Camanho, P., Mayugo, J., Dávila, C., 2007. A continuum damage model for composite laminates: Part II - Computational implementation and validation. Mech. Mater. 39 (10), 909–919. https://doi.org/10.1016/j.mechmat.2007.03.006.

Matzenmiller, A., Lubliner, J., Taylor, R., 1995. A constitutive model for anisotropic damage in fiber-composites. Mech. Mater. 20 (2), 125–152. https://doi.org/10.1016/0167-6636(94)00053-0.

Mazars, J., 1986. A description of micro- and macroscale damage of concrete structures. Eng. Fract. Mech. 25 (5–6), 729–737. https://doi.org/10.1016/0013-7944(86)90036-6.

Mihai, L.A., Woolley, T.E., Goriely, A., 2018. Stochastic isotropic hyperelastic materials: Constitutive calibration and model selection. Proc. R. Soc. A: Math., Phys. Eng. Sci. 474 (2211). https://doi.org/10.1098/rspa.2017.0858.

Mortazavian, S., Fatemi, A., 2015. Effects of fiber orientation and anisotropy on tensile strength and elastic modulus of short fiber reinforced polymer composites. Compos. Part B: Eng. 72, 116–129. https://doi.org/10.1016/j.compositesb.2014.11.041.

Naderi, M., Khonsari, M.M., 2013. Stochastic analysis of inter- and intra-laminar damage in notched PEEK laminates. Express Polymer Letters 7 (4), 383–395. https://doi.org/10.3144/expresspolymlett.2013.35.

Notta-Cuvier, D., Lauro, F., Bennani, B., Balieu, R., 2013. An efficient modelling of inelastic composites with misaligned short fibres. Int. J. Solids Struct. 50 (19), 2857–2871. https://doi.org/10.1016/j.ijsolstr.2013.04.031.

Nouri, H., Guessasma, S., Roger, F., Ayadi, A., Maitournam, H., 2017. Exploring damage kinetics in short glass fibre reinforced thermoplastics. Compos. Struct. 180, 63–74. https://doi.org/10.1016/j.compstruct.2017.07.096.

Pinho, S.T., Dávila, C.G., Camanho, P.P., Iannucci, L., Robinson, P., 2005. Failure Models and Criteria for FRP Under In-Plane or Three-Dimensional Stress States Including Shear Non-linearity, NASA/TM-2005-213530, Tech. rep., NASA Langley Research Center.

Puck, A., Shürmann, H., 1998. Failure analysis of FRP laminates by means of physically based phenomenological models. Compos. Sci. Technol. 58 (7), 1045–1067. https://doi.org/10.1016/S0266-3538(96)00140-6.

Reinoso, J., Catalanotti, G., Blázquez, A., Areias, P., Camanho, P.P., París, F., 2017. A consistent anisotropic damage model for laminated fiber-reinforced composites using the 3D-version of the Puck failure criterion. Int. J. Solids Struct. 126–127, 37–53. https://doi.org/10.1016/j.ijsolstr.2017.07.023.

Rolland, H., Saintier, N., Robert, G., 2016. Damage mechanisms in short glass fibre reinforced thermoplastic during in situ microtomography tensile tests. Compos. Part B: Eng. 90, 365–377. https://doi.org/10.1016/j.compositesb.2015.12.021.

Rolland, H., Saintier, N., Wilson, P., Merzeau, J., Robert, G., 2017. In situ X-ray tomography investigation on damage mechanisms in short glass fibre reinforced thermoplastics: Effects of fibre orientation and relative humidity. Compos. Part B: Eng. 109, 170–186. https://doi.org/10.1016/j.compositesb.2016.10.043.

Shen, Q., Zhu, Z., Liu, Y., 2019. Progressive failure analysis of scarf-repaired composite laminate based on damage constitutive model. Proc. Inst. Mech. Eng., Part L: J. Mater.: Design .Appl. 233 (2), 180–188. https://doi.org/10.1177/1464420716666400.

Simon, J.-W., Höwer, D., Stier, B., Reese, S., Fish, J., 2017. A regularized orthotropic continuum damage model for layered composites: intralaminar damage progression and delamination. Comput. Mech. 60 (3), 445–463. https://doi.org/10.1007/s00466-017-1416-1.

Sommer, D.E., Kravchenko, S.G., Denos, B.R., Favaloro, A.J., Pipes, R.B., 2020. Integrative analysis for prediction of process-induced, orientation-dependent tensile properties in a stochastic prepreg platelet molded composite. Compos. Part A: Appl. Sci. Manuf. 130, 105759. https://doi.org/10.1016/j.compositesa.2019.105759.

Song, J.-H., Wang, H., Belytschko, T., 2008. A comparative study on finite element methods for dynamic fracture. Comput. Mech. 42 (2), 239–250. https://doi.org/10.1007/s00466-007-0210-x.

Staber, B., Guilleminot, J., Soize, C., Michopoulos, J., Iliopoulos, A., 2019. Stochastic modeling and identification of a hyperelastic constitutive model for laminated composites. Comput. Methods Appl. Mech. Eng. 347, 425–444. https://doi.org/10.1016/j.cma.2018.12.036.

Stören, S., Rice, J., 1975. Localized necking in thin sheets. J. Mech. Phys. Solids 23 (6), 421–441. https://doi.org/10.1016/0022-5096(75)90004-6.

Su, X.T., Yang, Z.J., Liu, G.H., 2010. Monte Carlo simulation of complex cohesive fracture in random heterogeneous quasi-brittle materials: A 3D study. Int. J. Solids Struct. 47 (17), 2336–2345. https://doi.org/10.1016/j.ijsolstr.2010.04.031.

Tsai, S.W., Wu, E.M., 1971. A General Theory of Strength for Anisotropic Materials. J. Compos. Mater. 5 (1), 58–80. https://doi.org/10.1177/002199837100500106.

Wei, L., Zhu, W., Yu, Z., Liu, J., Wei, X., 2019. A new three-dimensional progressive damage model for fiber-reinforced polymer laminates and its applications to large open-hole panels. Compos. Sci. Technol. 182, 107757. https://doi.org/10.1016/j.compscitech.2019.107757.

Yang, Z.J., Su, X.T., Chen, J.F., Liu, G.H., 2009. Monte Carlo simulation of complex cohesive fracture in random heterogeneous quasi-brittle materials. Int. J. Solids Struct. 46 (17), 3222–3234. https://doi.org/10.1016/j.ijsolstr.2009.04.013.

Yoon, D., Kim, S., Kim, J., Doh, Y., 2019. Development and Evaluation of Crack Band Model Implemented Progressive Failure Analysis Method for Notched Composite Laminate. Appl. Sci. 9 (24), 5572. https://doi.org/10.3390/app9245572.

Yu, T.X., Shang, L.C., 1996. Plastic Bending. World Scientific.

Zheng, T., Guo, L., Huang, J., Liu, G., 2020. A novel mesoscopic progressive damage model for 3D angle-interlock woven composites. Compos. Sci. Technol. 185, 107894. https://doi.org/10.1016/j.compscitech.2019.107894.

Zhou, J., Wen, P., Wang, S., 2019. Finite element analysis of a modified progressive damage model for composite laminates under low-velocity impact. Compos. Struct. 225, 111113. https://doi.org/10.1016/j.compstruct.2019.111113.

Zhu, H., Gu, Y., Yang, Z., Li, Q., Li, M., Wang, S., Zhang, Z., 2020. Fiber distribution of long fiber reinforced polyamide and effect of fiber orientation on mechanical behavior. Polym. Compos. 41, 1531–1550. https://doi.org/10.1002/pc.25476.